

AperTO - Archivio Istituzionale Open Access dell'Università di Torino

Nanocomposites of Nickel Oxide and Zirconia for the Preparation of Photocathodes with Improved Performance in p-Type Dye-Sensitized Solar Cells

This is the author's manuscript

Original Citation:

Availability:

This version is available <http://hdl.handle.net/2318/1704070> since 2019-06-07T12:32:43Z

Published version:

DOI:10.1149/2.0691908jes

Terms of use:

Open Access

Anyone can freely access the full text of works made available as "Open Access". Works made available under a Creative Commons license can be used according to the terms and conditions of said license. Use of all other works requires consent of the right holder (author or publisher) if not exempted from copyright protection by the applicable law.

(Article begins on next page)

1 **Nanocomposites of nickel oxide and zirconia for the preparation of photocathodes with**
2 **improved performance in *p*-type dye-sensitized solar cells**

3 Matteo Bonomo^{a*}, Paolo Mariani^b, Francesco Mura^a, Aldo Di Carlo^{b,c} and Danilo Dini^{a*}

4 (a) *Department of Chemistry, University of Rome LA SAPIENZA, P.le A. Moro 5, 00185 Rome, Italy*

5 (b) *Dept. of Electronic Engineering, University of Rome "Tor Vergata", via del Politecnico 00133 Rome, Italy.*

6 (c) *National University of Science and Technology "MISIS", 4, Leninsky Prosp., Moscow 119049, Russian Federation*

7

8

DISCLAIMER

9 **THIS DOCUMENT IS THE NOT PAGINATED VERSION OF THE ARTICLE:**
10 **"Nanocomposites of nickel oxide and zirconia for the preparation of photocathodes with improved**
11 **performance in *p*-type dye-sensitized solar cells". PLEASE DOWNLOAD THE FINAL**
12 **PAGINATED VERSION AT <http://jes.ecsdl.org/content/166/8/D290>.**

13

14 **ABSTRACT**

15 In *p*-type dye sensitized solar cells (*p*-DSCs) with nickel oxide (NiO) based photocathodes one of
16 the main causes of their relatively poor photoconversion performances is the fast recombination
17 between the photoinjected holes in the valence band of the *p*-type semiconductor and the reduced
18 form of the redox shuttle (typically I⁻). As a matter of fact, recombination phenomena at the
19 NiO/electrolyte interface heavily limit both photovoltage and photocurrent. Different approaches
20 have been adopted to minimize such an unwanted process: these range from the pretreatment of the
21 electrode surface with NaOH to the employment of passivating organic molecules (e.g. CDCA) in
22 the sensitizing solution and/or in the electrolyte solution. The present contribution describes the
23 implementation of the addition of zirconia (ZrO₂) nanoparticles in nanostructured NiO films as anti-
24 recombination agent in *p*-DSCs due to the electro-inactivity of ZrO₂. ZrO₂ nanoparticles with
25 diameter, Ø, of 20 nm, and NiO nanoparticles with Ø < 50 nm were dispersed together in the paste
26 precursor for screen-printing. Different compositions of the mixture of NiO and ZrO₂ nanoparticles
27 were considered. From the combined analysis of the electrochemical and photoelectrochemical
28 properties of different nanocomposites it was concluded that the molar ratio ZrO₂/NiO had the
29 optimal range of 2-5 % for realizing photocathodes more efficacious than sole nanostructured NiO.
30 Among the nanocomposite photoelectrodes the one obtained from the inclusion of 2% of ZrO₂
31 nanoparticles produced the better photoelectrochemical performance being the short-circuit current
32 density $J_{SC} = 2.037 \text{ mA/cm}^2$ and the overall efficiency $\eta = 0.088\%$ when P1 is the sensitizer. These
33 results show an increase up to 40% compared to the un-modified NiO electrode. The unexpectedly
34 low efficiency of electrode with molar ratio of zirconia in nickel oxide of 5% was associated to an
35 insufficient dye-loading on NiO, in combination to the increase of the percentage of the
36 photoelectrochemically inert ZrO₂ additive. The electrochemical impedance spectroscopy (EIS)
37 data of the complete device under illumination confirmed that the improvement is mainly due to an
38 increase of the recombination resistance, R_{rec} , ongoing from sole nanostructured NiO ($R_{rec} = 56.3 \Omega$)
39 to the electrode obtained from the nanocomposite with molar ratio ZrO₂/NiO = 0.02 ($R_{rec} = 70.3 \Omega$).

40

41

42

43 * corresponding author, email: matteo.bonomo@uniroma1.it danilo.dini@uniroma1.it

44

45

46

47 INTRODUCTION

48

49 Among photovoltaic technologies the monocrystalline silicon-based devices and lead iodide based
50 perovskite solar cells are capable to reach conversion efficiencies up to 20% under solar
51 irradiation¹. When indoor illumination with diffuse features is considered as source of luminous
52 energy the dye-sensitized solar cell (DSC)² appears as the most effective choice despite the fact
53 that the highest efficiency of a DSC is below 15%³. More recently, Grätzel⁴ and co-workers
54 reported overall efficiency up to 30% when the source intensity is as low as 100 lux. Conversions
55 up to 40% could be theoretically achieved by creating a p-n junction⁵ (i.e. by coupling a photoanode
56 to a photocathode) when the solar radiation is considered as excitation source. Such a tandem
57 configuration would sensibly reduce also the costs of production of the corresponding device. The
58 theoretical limit of 40% is still far to be reached because of the generally poor performance of
59 photocathodes. To our knowledge, the best performance reported so far for a *p*-type DSC (*p*-DSC)
60 is lower than 2% under 1 Sun of illumination⁶. One of the main causes of this is the fast
61 recombination reaction that occurs between the photoinjected holes in the valence band (VB) of the
62 photocathode (usually made of NiO)⁷⁻¹⁰ and the reduced form of the redox shuttle (typically the
63 iodide anion)¹¹⁻¹³. In fact, recombination phenomena at the NiO/electrolyte interface heavily limit
64 both photovoltage and photocurrent. The photoinjected holes are mainly localized onto NiO surface
65 in correspondence of the electron-deficient Ni³⁺ sites. Different approaches have been adopted to
66 minimize such an unwanted reaction. The rational design of a sensitizer with bulky
67 substituents^{6,14,15} could help to keep iodide distant from the holes localized on the electrode surface.
68 The implementation of a NiO compact layer has been proved to reduce recombination phenomena
69 at the electrolyte/FTO interface¹⁶⁻¹⁸. Metal-doping or UV irradiation of NiO electrode are feasible
70 approaches to tune the opto-electronic properties of photocathode but are as not effective in
71 reducing the interfacial recombination¹⁹⁻²¹. An alternative route is the direct modification of the
72 photocathode. In a previous paper we showed that the treatment of NiO surface with soda has a
73 twofold effect: it reduces the surface concentration of superficial Ni³⁺ sites and passivates the NiO
74 surface prior sensitization²². The success of this method has been confirmed by the achievement of
75 a less dark film. Unfortunately, the reduction of the number of Ni³⁺ sites lowered also the amount of
76 loaded sensitizer leading to a less performing device (lower photocurrent). We also tested CDCA
77 (chenodeoxycholic acid) in squaraines-based *p*-DSC²³. In that work CDCA (acting as both
78 disaggregating and passivating agent) was added in the sensitizer solution with a concentration of
79 20 mmol. The overall efficiency was enhanced by 25% due to the depression of dye aggregation.
80 Nevertheless, the amount of chemisorbed dye was lowered because of the competition between
81 sensitizer and CDCA in binding Ni³⁺ sites. To avoid the latter phenomena, Odobel *et al.*²⁴ dissolved
82 CDCA (50 mM) in the electrolyte. They reported an enhancement of the 20 % of the conversion
83 efficiency due mainly to a higher V_{OC} whereas the J_{SC} was substantially unchanged. The
84 employment of an insulating layer of Al₂O₃ was proposed by Uehara and coworkers²⁵ but it
85 diminished the electron injection of surface chemisorbed sensitizer more than the desired
86 recombination phenomena Natu and co-authors reported the implementation of a more efficient
87 Al₂O₃ insulating layer directly deposited onto the NiO electrode by Atomic Layer Deposition²⁶.
88 Yet, the enhancement of photoelectrochemical properties is modest. As far as we are aware, no
89 research group previously attempted the nanometric approach in the framework of DSCs with the
90 preparation of the nanocomposites here reported. In particular, throughout this work we described,
91 for the first time, the employment of ZrO₂ nanoparticles, NPs, with diameter $\varnothing < 20$ nm) as not
92 electroactive additive in NiO electrodes for *p*-DSC application. ZrO₂ is an insulating oxide with a
93 bandgap higher than 5 eV. We expect that the presence of zirconia nanoparticles, i.e. a
94 nanostructured version of ZrO₂ with strong tendency of being finely dispersed on the electrode
95 surface, diminishes the portion of NiO exposed to the electrolyte thus diminishing the probability
96 with which Ni³⁺ sites on the surface recombine with the redox shuttle. The effect of NiO dilution
97 imparted by of zirconia nanoparticles on the electrode surface brings necessarily about the

98 consequent minimization of recombination phenomena at the electrode/electrolyte interface as well
99 as flux of photoinjected charges in the photocathode. The purpose of this study is to evaluate to
100 which extent the presence of ZrO₂ NPs favors the suppression of recombination without being
101 excessively detrimental against dye-loading and photoinjection on the NiO portions of the
102 nanocomposite. ZrO₂ has been chosen because of its chemical inertness and long-term stability. The
103 formation of a mixed oxide of nickel and zirconium with a structure distinct from the ones of NiO
104 and ZrO₂ has not been evidenced (vide infra)²⁷. Therefore, the attainment of a solid solution from
105 the mixing and the sintering of NiO and ZrO₂ NPs is reasonably excluded. On these bases we
106 expect that the nanocomposites are actually constituted by two segregated oxides.

107

108 **EXPERIMENTAL PART**

109

110 The chemicals ethylcellulose, α -terpineol, NiO nanopowders, ethanol and acetonitrile (ACN) were
111 purchased from Fluka or Sigma-Aldrich whereas ZrO₂ nanoparticles were purchased from US
112 Research Nanomaterials. All chemicals were used without any further treatment of purification.

113 The experimental procedure to produce NiO/ZrO₂ slurry consists on a modified version of the one
114 reported in our previous paper^{28,29}: an ethanol solution of NiO nanopowders (6 g), ZrO₂
115 nanospheres (variable amount), α -terpineol as solvent (20 g) and ethylcellulose as crosslinker were
116 mixed together under continuous stirring. Then this solution was slowly heated at 50 °C to let
117 completely evaporate the solvent. The resulting slurries were screen-printed over 2.2 mm thick
118 FTO/glass substrates (TEC7 from NSG), which were previously cleaned in an ultrasonic bath with
119 acetone for 10 min and successively with isopropyl alcohol for 10 min. The electrodes with
120 geometrical area of 0.36 cm², were annealed at 450 °C in oven for 30 minutes. The thickness of the
121 annealed samples ranged between 2 and 3 μ m (evaluated with a Dektak 150[®] profilometer from
122 Veeco). The morphology has been investigated with a FESEM Auriga Zeiss Field Emission. EDX
123 (EDX Quantax Bruker, Resolution 123 eV (Mn K α)) was employed for the elemental analyses. The
124 amount of added ZrO₂ varied from 0 (pure NiO) to 856 mg (corresponding to the molar ratio
125 ZrO₂/NiO = 0.11). Six slurries have been prepared with different values of ZrO₂/NiO molar ratio:

126

- 127 • Pure NiO as reference
- 128 • ZrO₂/ NiO = 0.001, with 8 mg of ZrO₂
- 129 • ZrO₂/ NiO = 0.010, with 85.6 mg of ZrO₂
- 130 • ZrO₂/ NiO = 0.020, with 171.2 mg of ZrO₂
- 131 • ZrO₂/ NiO = 0.053, with 428 mg of ZrO₂
- 131 • ZrO₂/ NiO = 0.111, with 856 mg of ZrO₂

132 The resulting slurries were chemically and physically stable for several months in ambient
133 conditions. Throughout the paper, each electrode made starting from these slurries has been named
134 as NiO_ZrO₂_X where X represents the ZrO₂/NiO molar ratio.

135 The electrochemical characterization of ZrO₂/NiO samples consisted in the recording of cyclic
136 voltammeteries (CVs), and electrochemical impedance spectra with Autolab potentiostat/galvanostat
137 Mod. PGSTAT12[®] from Metrohm. PGSTAT was remotely controlled from a computer by means
138 of the software Nova 1.9. The electrochemical cell had a three-electrode configuration with NiO
139 (either bare or ZrO₂-modified as nanocomposite) as working electrode, a platinum wire as the
140 counter-electrode and Ag/AgCl electrode as the reference electrode. The supporting electrolyte was
141 0.1 M LiClO₄ in ACN. With regard to the CV measurements the applied potential has been varied
142 from -0.27 to 1.13 V with a variable scan rate (10, 20, 50, 100 or 200 mV*s⁻¹). Impedance spectra
143 were recorded in the same experimental set up by applying a frequency value ranging from 100
144 KHz to 0.1 Hz with a potential amplitude of stimulus of 20 mV.

145 WAXS experiments were carried out on a Bruker D8 Advance with DaVinci design diffractometer
146 (angle dispersive). The diffractometer is equipped with a Cu K α X-Ray tube ($\lambda = 1.5406 \text{ \AA}$). The
147 instrument is fitted with focusing Göbel mirrors along the incident beam and Soller slits on both
148 incident and diffracted (radial) beams. Data were measured in step-scan mode in the 20-80° angular
149 range with a step of 0.02° within the Bragg-Brentano para-focusing geometry. Only the incident
150 beam slit was closed (0.2 mm width), while the diffracted beam slit was left open. The samples
151 were held on microscope slides within a humidity-controlled chamber purposely developed. The
152 scattered intensity was gathered with the Lynxeye XE Energy-Dispersive 1-D detector.

153 For the assembly of the DSC the different electrodes were sensitized by dipping them in a P1³⁰
154 solution (0.3 mM in ACN) for 16 hours. The electrodes were rinsed with ACN to remove the excess
155 of not chemisorbed dye. Optical transmittance of sensitized photocathodes was measured with a
156 double ray spectrometer [UV-2550 by Shimadzu, Kyoto (JP)].

157 Bare and P1-sensitized photocathodes were assembled in a sandwich configuration with platinised-
158 FTO as counter-electrode. A double layer of Platinum (3D-nano) was screen-printed onto the
159 counter-electrodes. The first layer was dried at 120 °C for 10 min before printing the second one.
160 As the first, the second layer was dried at 120°C in order to burn the solvents. Successively the
161 counter-electrodes were fired at 480 °C in oven for 30 min for the thermal reduction of the Pt
162 precursor³¹. A thermoplastic resin (Surlyn®, from Dupont), was used as spacer and sealant. The
163 electrolyte (Iodolyte-H from Solaronix) was injected inside the two sandwiched electrodes by
164 vacuum backfilling technique through a drilled hole -one for each cell- in the Surlyn® mask. These
165 holes were sealed with a specific UV-curable resin (TB3035B from ThreeBond®).

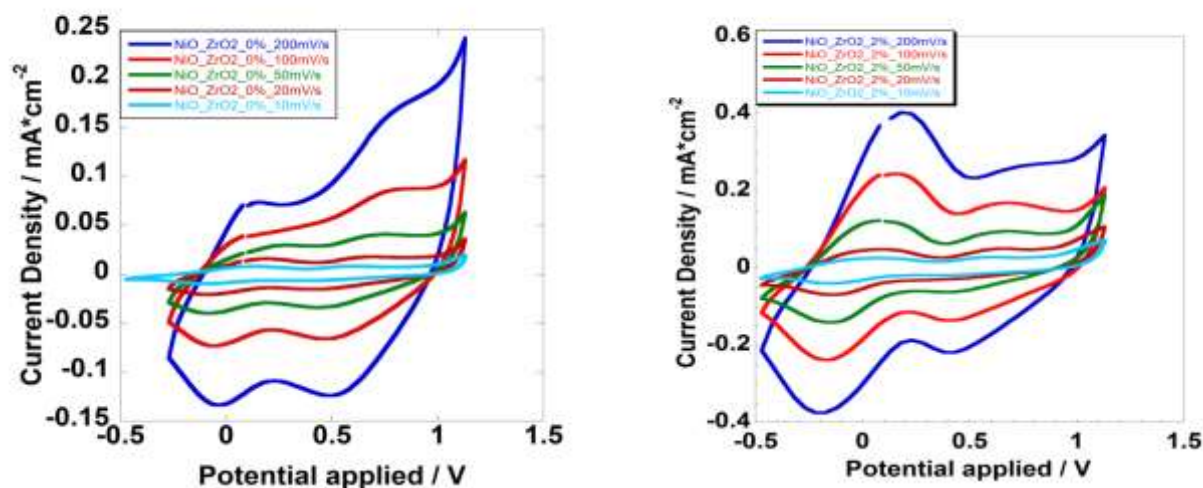
166 Photoelectrochemical characterization of the *p*-DSCs consisted in the recording of the JV
167 characteristic curves, incident photon-to-current conversion efficiency (IPCE) spectra and in-light
168 EIS data. All the measurements were recorded with a Sun Simulator AM 1.5G at 1 SUN (Incident
169 Power = 1000 W m⁻²) using a Keithley 2420 as a source-meter in ambient conditions. The light
170 source was calibrated with s SKS1110 sensor (Skye Instruments Ltd).

171

172 **RESULTS AND DISCUSSION**

173 Figure 1 shows the voltammograms of bare NiO and NiO_ZrO₂_2%, which were recorded within
174 the potential range -0.5 - 1 V vs Ag/AgCl at different scan rates (range:10-200 mV s⁻¹). In both
175 series of CVs two main peaks are observed: the peak at lower potential corresponds to the reversible
176 solid state oxidation of NiO with occurrence of Ni²⁺ → Ni³⁺ + 1 e⁻ (named O1); the peak at higher
177 potential is assigned to the formal oxidation of preexisting Ni³⁺ sites into Ni⁴⁺ (named O2)³². The
178 current peak of O1 was more than doubled in going from bare NiO to the sample NiO_ZrO₂_2%.
179 Moreover, a sensible variation of the O2/O1 ratio is observed in the compared analysis of NiO and
180 NiO_ZrO₂_2% electrodes being the O2 peak less pronounced when the electrode is
181 doped/combined with ZrO₂. This combination of findings leads us to suppose that the presence of
182 zirconia as a fine dispersion diminishes the surface concentration of Ni(III) in the *as deposited*
183 sample. Beside the diminution of the portion of defective NiO, i.e. the portion containing Ni(III)
184 sites, the presence of zirconia would favor the relative increase of the surface concentration of
185 Ni(II) sites with respect to bare NiO. The latter statements are going to be verified in a successive
186 study through the adoption of the XPS technique for the speciation of these NiO/ZrO₂
187 nanocomposites. In Table 1, the charge density exchanged during the occurrence of O1 and O2 as
188 well as their relative ratio are reported. The O2/O1 ratio decreases regularly upon increase of ZrO₂
189 content up to the composition NiO_ZrO₂_2%. When the ZrO₂/NiO ratio becomes higher (samples
190 NiO_ZrO₂_5% and NiO_ZrO₂_10%), the ratio O2/O1 increases again. This is a consequence of the
191 fact that zirconia should form aggregates at relatively high concentrations thus becoming a

192 segregated phase, i.e. ZrO₂ is not longer homogeneously dispersed in the form of nanoparticles
 193 within the NiO nanostructure. In the aggregated state zirconia, i.e. the component representing the
 194 passivating and non-electroactive agent of the composite, becomes less efficient in blocking the
 195 Ni³⁺ sites. Simultaneously, the presence of ZrO₂-based macrostructure on the NiO surface
 196 decreases the active surface area of the electrode. In this context the presence of ZrO₂-based
 197 macrostructure on NiO surface can explain both the detrimental effect on NiO electrochemical
 198 activity of the electrode as well as the increase in O₂/O₁ ratio.



199

200 Figure 1. CVs of (right) NiO bare and (left) NiO_ZrO₂_2% at different scan rates [10 mV/s (light blue), 20 mV/s (red), 50 mV/s
 201 (green), 100 mV/s (light red) and 200 mV/s (dark blue)]. The supporting electrolyte was 0.1 M LiClO₄ in ACN. CE was a
 202 platinum rod and RE is SSE (+0.220 mV vs NHE).

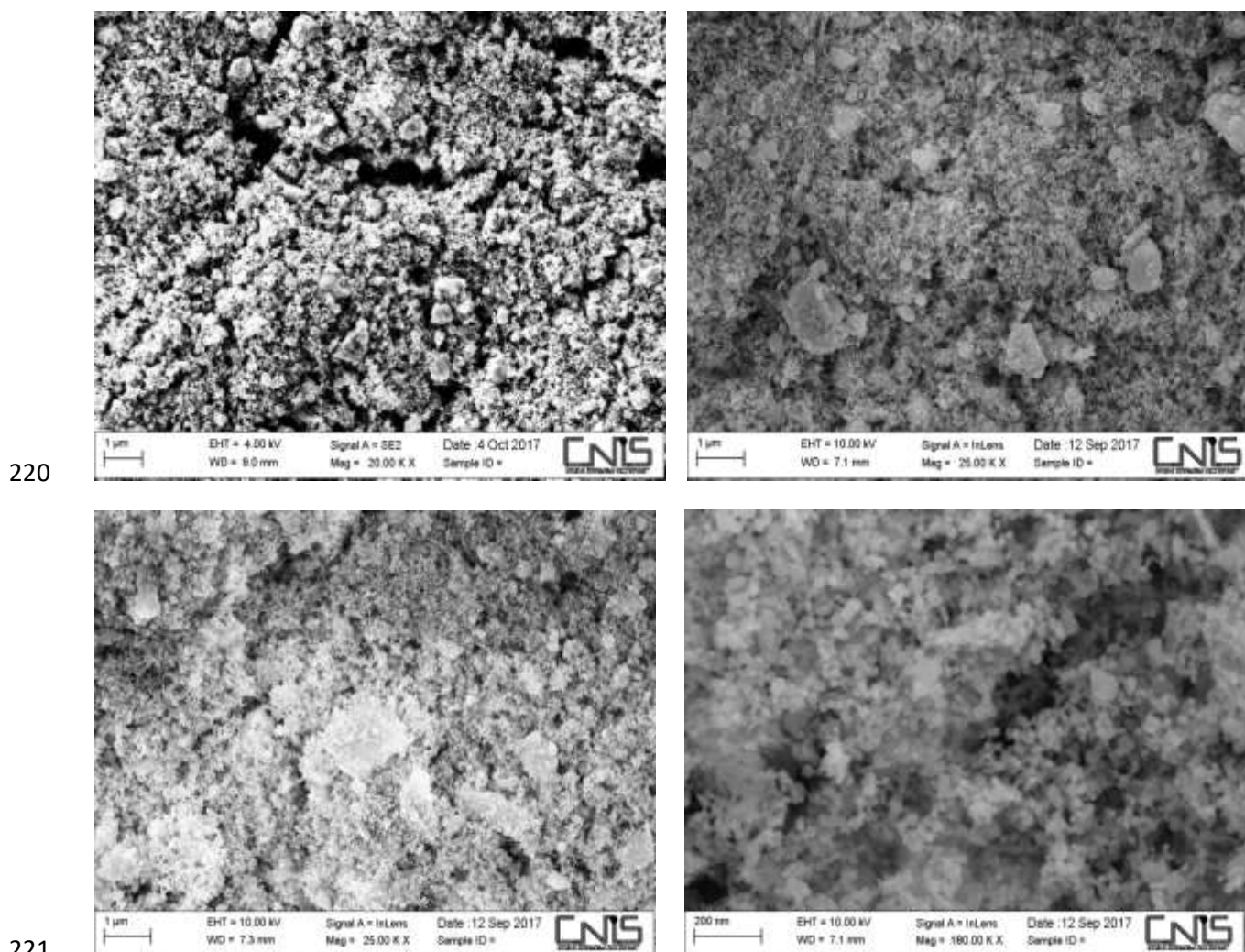
Electrode	O1 peak (mC cm ⁻²)	O2 peak (mC cm ⁻²)	O2/O1 (%)
NiO	0.195	0.207	106.2
NiO_ZrO ₂ _0.1%	0.206	0.178	86.4
NiO_ZrO ₂ _1%	0.461	0.144	31.2
NiO_ZrO ₂ _2%	0.990	0.200	20.2
NiO_ZrO ₂ _5%	0.686	0.162	23.3
NiO_ZrO ₂ _10%	0.096	0.033	34.3

203 Table 1. Charge density exchanged during the processes identified as O1 and O2 and relative ratio.

204 From Table 1, it could be evidenced that NiO_ZrO₂_2% showed both the better electrochemical
 205 activity, i.e. the higher value of exchanged charge, and the relatively lower extent of Ni³⁺ in the
 206 sample being this characteristic associated with the lower O₂/O₁ ratio. Because of that, sample
 207 NiO_ZrO₂_2% appeared as the most suitable electrode to be employed as photocathode in a *p*-
 208 DSC³³.

209 For the detection of the eventual presence of these ZrO₂-based macrostructures we performed
 210 combined SEM-EDX measurements. SEM (Figure 2) evidenced all samples possessed a quite open
 211 morphology with a lot of nanometer size voids: such a morphological feature is essential to assure a
 212 sufficiently high dye-loading for DSC purposes. The presence of ZrO₂ macrostructures was detected
 213 in all samples. For the determination of the actual chemical nature of the macrostructures we
 214 analyzed the elemental distribution on the electrode surface with Energy Dispersive X-ray (EDX,
 215 figure 3) spectroscopy. The analysis concerned the search of the elements Ni, O and Zr. The

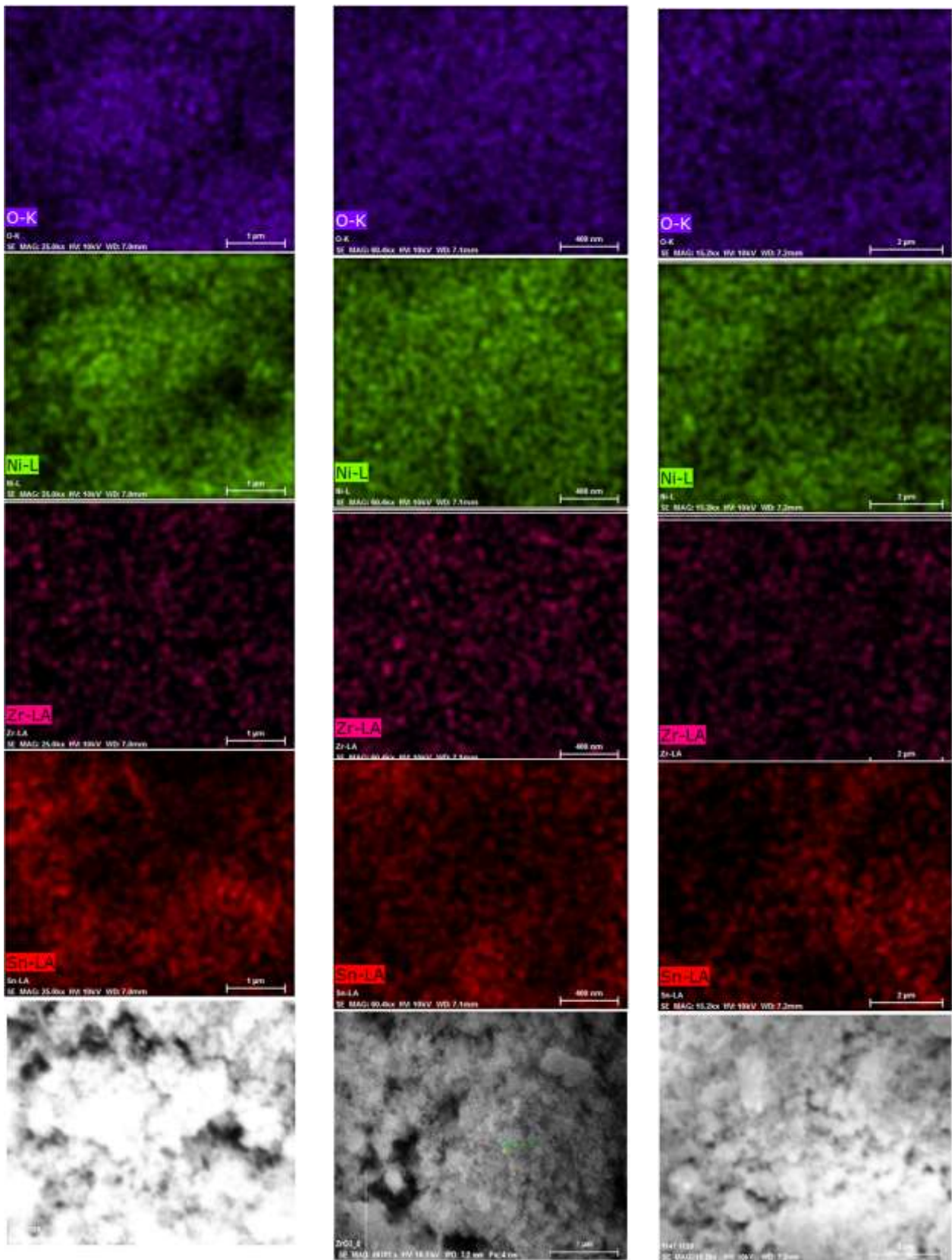
216 eventual presence of Sn from FTO substrate was also checked to evaluate the porosity of the screen-
217 printed electrodes. Are here shown the SEM and EDX images of NiO, NiO_ZrO₂_2% and
218 NiO_ZrO₂_5%. Additional images have been collected in the supporting information (Figures
219 ESII-ESI4).



222 **Figure 2.** SEM image of the NiO electrodes differing for the amount of ZrO₂: (top left) NiO; (top right) NiO_ZrO₂_2% and (bottom
223 left) NiO_ZrO₂_10%. A magnification of NiO_ZrO₂_2% has been shown (bottom right) to evidence the dispersion of ZrO₂ NPs onto
224 the NiO surface.

225 By the comparison of images in Figure 2 and ESIX, one can see that a ZrO₂/NiO molar ratio higher
226 than 2% leads to the growth of some macrostructures. The latter feature became more evident in
227 NiO_ZrO₂_10%. Interestingly, the presence of nanoparticles randomly dispersed onto the electrode
228 surface was evidenced too with EDX spectroscopy. EDX confirmed also that the ZrO₂
229 macrostructures were formed by the aggregation of ZrO₂ NPs in the samples with the largest
230 concentration of zirconia. As shown in figure ESIX, a concentration of Zr and a lower amount of
231 Ni was revealed in the analyzed area. Moreover, this structure is not porous since the signal of Sn
232 could not be detected. The presence of superficial Zr could not be found in NiO_ZrO₂_0.1% (Figure
233 ESII) because of the too high dispersion of ZrO₂ NPs, which is below the sensitivity of the EDX
234 instrument (0.065 mmol per unit area). The signal of Sn was detected for all nanocomposites with
235 molar content of Zr smaller than 10% (See ES15).

236



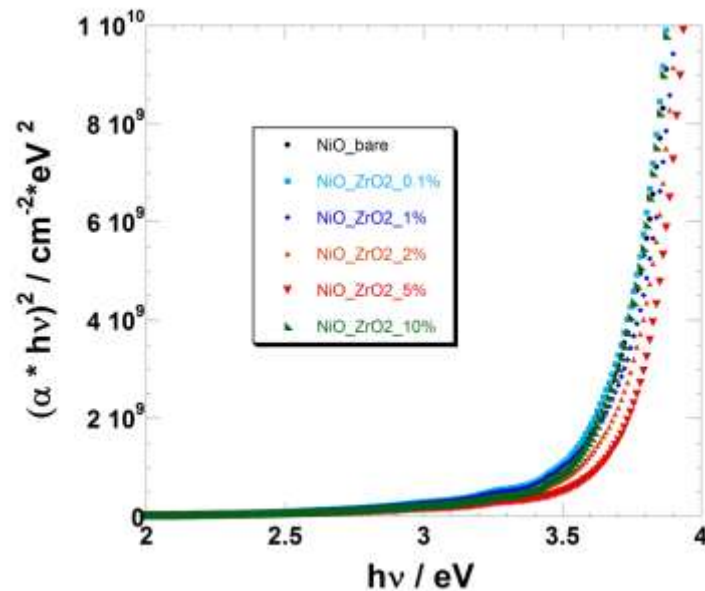
237

238 **Figure 3.** EDX images of (left column) NiO_ZrO₂_1%, (middle column) NiO_ZrO₂_2% and (right column) NiO_ZrO₂_5%. The
 239 surface distribution of different elements has been marked with different colors: violet-blue = O (first row of images); green = Ni
 240 (second row of images); pink = Zr (third row of images); red = Sn (fourth row of images). The bottom row represents the
 241 morphology of the three different samples of nanocomposites here considered.

242

243

244 The *Tauc's plot* was employed to determine the optical band gap of not sensitized electrodes upon
245 variation of zirconia content (Figure 4).



246

247 **Figure 4.** Tauc's plot for the extrapolation of the optical bandgap in the different nanocomposites of NiO and ZrO₂. Black circles:
248 NiO; light blue squares: NiO_ZrO₂_0.1%; dark blue diamonds: NiO_ZrO₂_1%; orange triangles: NiO_ZrO₂_2%; red triangles:
249 NiO_ZrO₂_5%; green triangles: NiO_ZrO₂_10%.

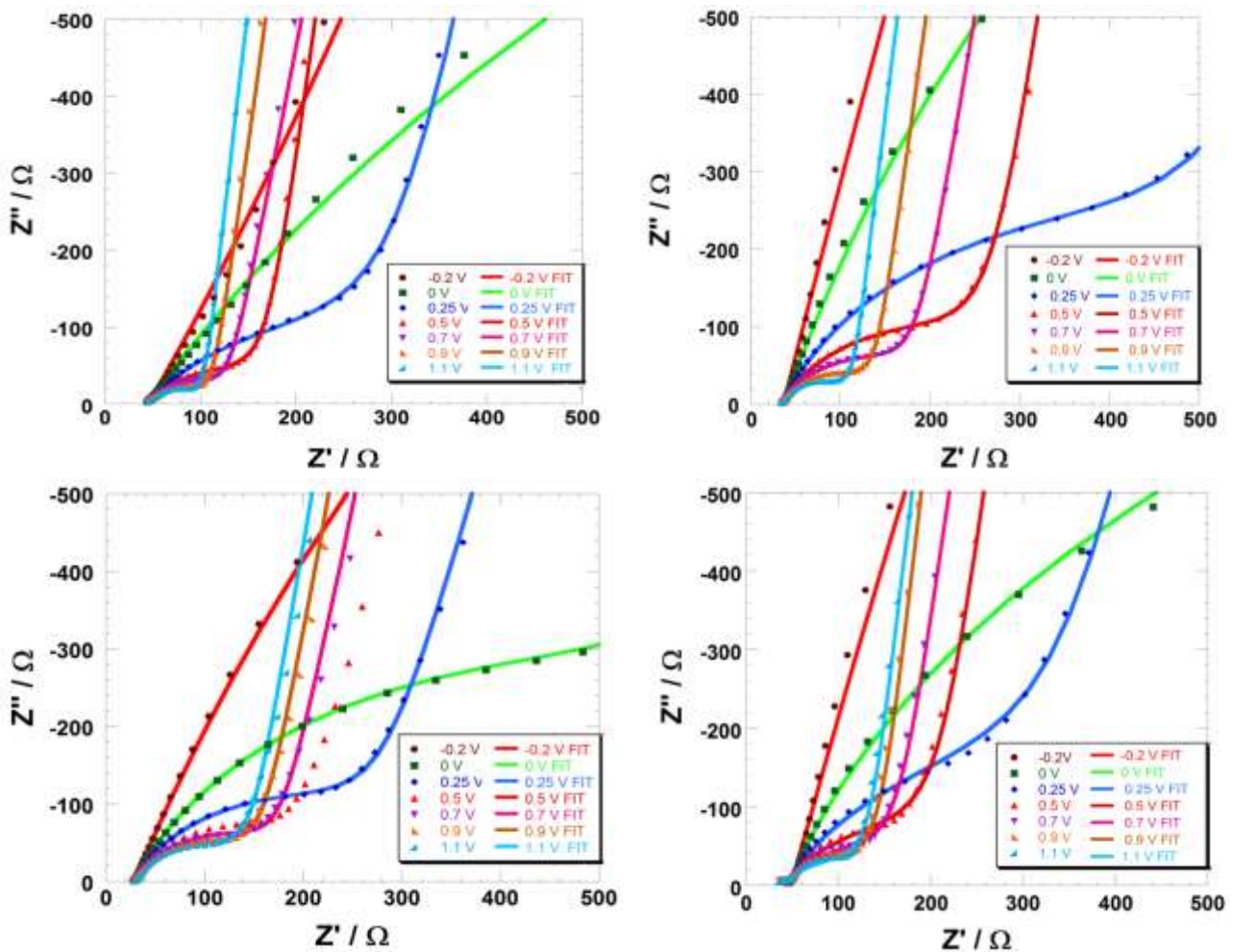
250 In the present case, the bandgap E_g for this series of nanocomposites tends to increase
251 monotonically on going from NiO to NiO_ZrO₂_5% whereas the bandgap of NiO_ZrO₂_10% is
252 very similar to the one of NiO. More precisely, the calculated bandgap is 3.62, 3.61, 3.68, 3.71, 3.75
253 and 3.63 for NiO, NiO_ZrO₂_0.1%, NiO_ZrO₂_1%, NiO_ZrO₂_2%, NiO_ZrO₂_5% and
254 NiO_ZrO₂_10%, respectively. The blue-shifted E_g of the ZrO₂/NiO electrode with respect to NiO
255 leads to more transparent films of the nanocomposites with respect to NiO in the visible range. A
256 larger number of defects in the lattice corresponds to a system with a tighter the optical band gap.

257 Electrochemical impedance spectra were recorded in a three-electrode cell configuration in dark
258 condition in order to avoid any modification induced by the eventual photoactivity of NiO working
259 electrode. The applied potential ranged in the interval -0.2 - 1.1 V (*vs* Ag/AgCl) (Figure 5).
260 Experimental data have been fitted with the equivalent circuit depicted in Figure ES15: the first
261 element simulates charge-transfer phenomena occurring at the electrode/electrolyte interface whilst
262 the second accounts for the charge transport through the electrode with its characteristic charge
263 transport resistance and capacitance. In the present context, we focus our attention and discuss
264 mainly the former type of phenomenon, i.e. interfacial charge transfer since this represents the
265 process at the basis of recombination in the actual *p*-DSC device and constitutes the problem which
266 is here tackled through the introduction of nanocomposites of electroactive NiO and
267 electrochemically inert ZrO₂. The electrolyte composition in the experiments of electrochemical
268 impedance is the same as the one employed in the experiments of cyclic voltammetry.

269 In Table 2 R_{CT} represents the charge transfer (CT) resistance at the electrolyte/electrode interface,
270 C_{INTER} is the double layer capacitance whereas $C_{electrode}$ is the capacitance of the electrode layer. EIS
271 data evidenced that R_{CT} diminishes with the applied potential irrespective of the amount of zirconia
272 in the electrode. This is expected since the increase of the applied potential is accompanied by the
273 concomitant increase of the number of holes, i.e. the mobile charged species that are injected

274 electrochemically in the film of NiO during its oxidation. Beside the improvement of the charge
 275 transfer properties these holes contribute to the double layer capacitance C_{INTER} at
 276 electrode/electrolyte interface and to the capacitance $C_{electrode}$ of the electrode bulk. When CT is
 277 relatively fast it promotes the formation of a diffuse double layer instead of a compact one. The R_{CT}
 278 values decrease sharply when the applied potential approaches the values of NiO redox processes,
 279 i.e. between 0 and 0.25 V and between 0.5 and 0.7 V for $Ni^{2+} \rightarrow Ni^{3+}$ and $Ni^{3+} \rightarrow Ni^{4+}$ reactions,
 280 respectively. A similar behaviour has been already reported for NiO when is polarized in aqueous
 281 electrolytes³⁴. Among the various formulations of the nanocomposites in the pristine state, the
 282 system NiO_ZrO₂_2% showed the lowest R_{CT} (2218 Ω), and the largest values of the capacitive
 283 terms $C_{electrode}$ and C_{INTER} . These findings denote the existence of a quite defective material with a
 284 relatively high number of native charges in starting NiO_ZrO₂_2%. Upon completion of the
 285 oxidation processes ($E_{appl} = 1.10$ V vs Ag/AgCl) NiO_ZrO₂_2% presented also the largest value of
 286 R_{CT} (twice the value of bare NiO one): this is an indication of the stronger tendency of this
 287 particularly formulation of nanocomposite to suppress efficaciously recombination at the
 288 electrode/electrolyte interface with respect to the other combinations.

289



290

291

292 **Figure 5.** EIS data of (top left) NiO bare, (top right) NiO_ZrO₂_1%, (bottom left) NiO_ZrO₂_2% and (bottom right) NiO_ZrO₂_10%
 293 at different applied potential: -0.20 (dark red circles), 0.00 (dark green squares), 0.25 (dark blue diamonds), 0.50 (red triangles), 0.70
 294 (purple triangles), 0.90 (orange triangles) and 1.10 V vs Ag/AgCl (light blue triangles). The fittings have been reported as full lines.

295

296

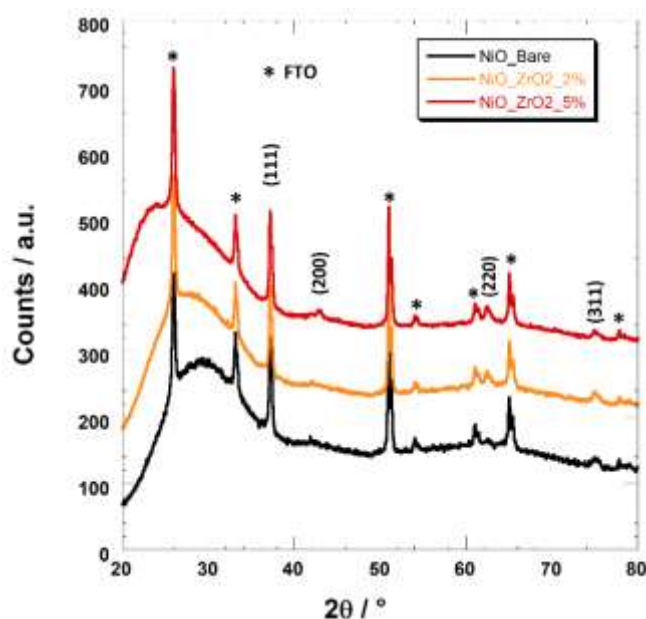
	E / V vs Ag/AgCl	-0.20	0.00	0.25	0.50	0.70	0.90	1.10
NiO	R_{CT} / Ω	3715	1942	284	131	88	71	62
	C_{INTER} / μF	33.2	28.6	24.4	16.2	11.9	10.2	9.2
	C_{electrode} / μF	53.8	178.2	198.5	212.1	225.2	236.7	239.8
NiO_ZrO ₂ _0.1%	R_{CT} / Ω	3134	707	312	198	131	99	84
	C_{INTER} / μF	37.3	31.7	22.3	20.7	14.1	13.5	12.4
	C_{electrode} / μF	55.3	184.4	218.8	232.2	242.6	252.9	254.6
NiO_ZrO ₂ _1%	R_{CT} / Ω	2540	635	328	237	151	126	102
	C_{INTER} / μF	43.8	35.9	26.1	21.3	17.9	15.3	13.6
	C_{electrode} / μF	65.1	223.2	293.2	301.2	332.9	336.5	362.8
NiO_ZrO ₂ _2%	R_{CT} / Ω	2218	593	248	179	148	130	119
	C_{INTER} / μF	49.7	33.7	26.5	20.4	17.6	15.6	14.8
	C_{electrode} / μF	170.1	332.2	383.3	393.8	436.4	446.0	470.7
NiO_ZrO ₂ _5%	R_{CT} / Ω	2649	741	346	264	164	133	112
	C_{INTER} / μF	47.9	36.0	26.5	19.7	17.3	15.1	13.8
	C_{electrode} / μF	132.0	248.9	340.8	342.8	367.9	384.6	402.3
NiO_ZrO ₂ _10%	R_{CT} / Ω	4135	1002	422	280	136	117	108
	C_{INTER} / μF	46.6	31.7	23.7	17.2	14.4	12.6	11.7
	C_{electrode} / μF	72.2	191.8	198.6	204.6	228.9	230.9	236.9

297
298

Table 2. Electric parameters derived from the fit of experimental impedance spectra. The errors on the fitting parameters are less than 3%.

299 In order to check the crystallographic structure of our modified samples and the eventual arising of
300 some NiO/ZrO₂ mixed phase, we performed X-Ray Diffraction measurements. The results have
301 been reported in figure 6: as one can see, the XRD spectrum of bare NiO (JCPDS card No. #47-
302 1049) shows one main peak corresponding to the 111 plane (at 37.2°) and a smaller peak at 75.1°
303 corresponding to the 311 plane. All the peak indexed with * arising from the FTO employed as
304 substrate³⁵. The addition of ZrO₂ NPs leads to a slight modification of the XRD pattern: two small
305 peaks could be evidenced at 42.8° and 62.5° ascribable to the 200 and 220 plane of cubic NiO
306 (JCPDS card No. #47-1049), respectively. Furthermore, there is not any evidence of peak due to
307 ZrO₂ or NiO/ZrO₂ mixed phases. The XRD pattern of monoclinic ZrO₂ usually presents two main
308 peaks at 28.1° (110) and 31.4° (111), JCPDS card No. #78-1807, whereas the spectrum of
309 tetragonal zirconia is composed by three main peaks centred at 30.2° (101), 50.2° (112) and 60.2°
310 (211), JCPDS card No. #79-1769. The absence of any crystallographic peak of ZrO₂ is ascribable to
311 the homogenous dispersion of the nanoparticles (figure 3) that not allow the occurrence of large
312 ZrO₂ crystallographic domains. Therefore, the effect of the addition of ZrO₂ results in the growth of
313 the NiO matrix in additional crystalline planes. More interestingly, the rise of NiO/ZrO₂ mixed
314 phase could be completely ruled out.

315

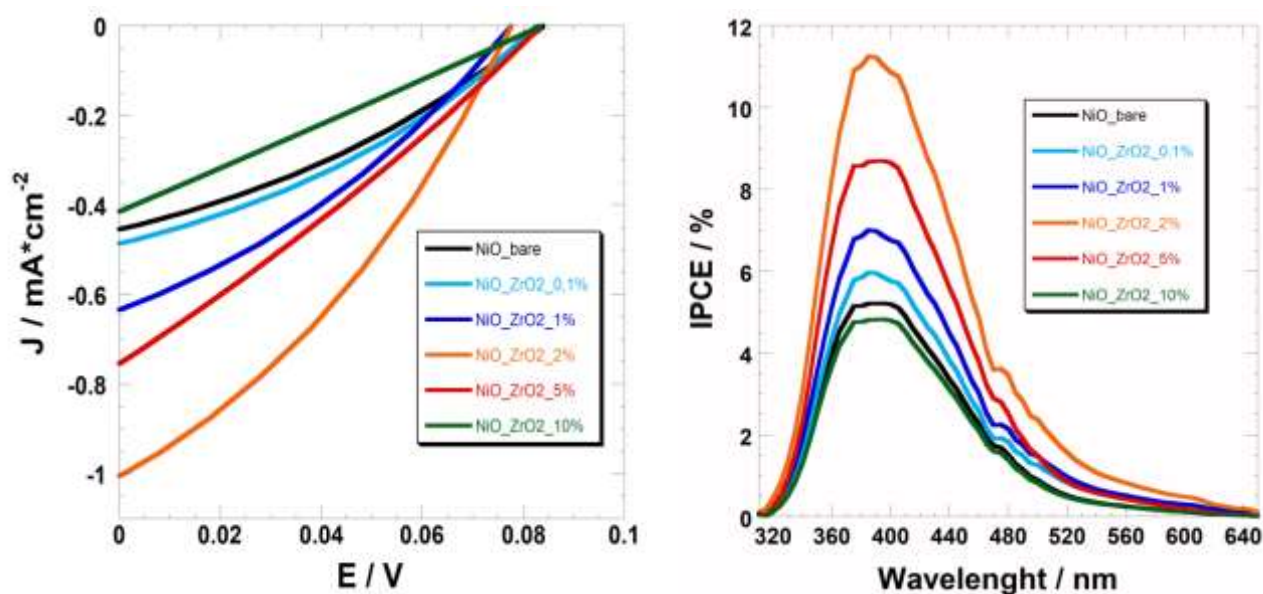


316

317 **Figure 6.** XRD spectra of bare NiO (black line), NiO_ZrO2_2% (orange line) and NiO_ZrO2_5% (red line) films. The peak due to the
 318 presence of crystalline NiO are indexed by the name of the corresponding plane. *-indexed peak refers to FTO substrate.

319 The *JV* curves of the *p*-DSCs with the six formulations here considered have been recorded for both
 320 pristine and P1-sensitized electrodes to stress eventual changes in the operating features of the NiO-
 321 based electrode after sensitization. When dye is not loaded onto the NiO surface, the only accessible
 322 pathway to produce photocurrent is the excitation of an electron from the VB of NiO to its CB at
 323 the approximate wavelength of excitation $\lambda_{exc} \approx 320$ nm. To reduce the current losses due to
 324 recombination phenomena, Ni³⁺ sites should be inaccessible to the reducing species that are present
 325 in solution: the implementation of ZrO₂ NPs avoids that the surface of nickel oxide with its
 326 recombination defects is fully exposed to the electrolyte. The practical effect of the introduction of
 327 ZrO₂ NPs is the increase in the powered photocurrent: +123% on going from pristine NiO to
 328 NiO_ZrO₂_2% (Figure 7 and Table 3) accounting for a huge decrease in recombination phenomena.
 329 NiO and NiO_ZrO₂_2% produced a photocurrent of 0.448 mA*cm⁻² and 0.994 mA cm⁻² ,
 330 respectively. The trend of photocurrent is not monotonic: it reached its maximum when ZrO₂ to
 331 NiO have a molar ratio of 2% and it decreased for NiO_ZrO₂_5% and NiO_ZrO₂_10% ($J_{SC} = 0.747$
 332 and 0.414 mA cm⁻², respectively). This trend is in accordance with the CV and EIS data (*vide*
 333 *supra*). Such a combination of findings shows how revealing is the analysis of the electrochemical
 334 properties in case of nanostructured NiO electrodes for the successive evaluation of their
 335 photoelectrochemical performance. When compared to sole NiO, the sample of NiO_ZrO₂_0.1%
 336 does not show any significant difference in terms of electrochemical and photoelectrochemical
 337 behavior due to the fact that zirconia NPs are too dispersed to effectively influence the
 338 (photo)electrochemical properties of the corresponding nanocomposite electrode. NiO_ZrO₂_1%,
 339 NiO_ZrO₂_2% and NiO_ZrO₂_5% manifested similar electrochemical behavior and displayed
 340 similar morphologies. In case of NiO_ZrO₂_1% such a concentration of ZrO₂ does not allow a good
 341 dispersion of the nanoparticles throughout the NiO film whereas molar percentage values higher
 342 than 2% causes the formation of pure ZrO₂ macrostructure that can prevent the exposure of the Ni³⁺
 343 sites. Among the doped electrode NiO_ZrO₂_10% showed the worst performance: the electrode
 344 mainly suffered for an extremely low Fill Factor (FF $\approx 25\%$). Such a result could be ascribed to the
 345 presence of large aggregates of zirconia that produce as main effect the inhibition of the process of

346 photoinjection rather than preventing recombination. Moreover, the electrode formulation
347 NiO_ZrO₂_5% showed a relatively low FF ($\approx 28\%$) too. Open circuit potential (V_{OC}) values ranged
348 from 78 to 85 mV without showing any clear trend with the amount of dispersed zirconia.



349

350 **Figure 7.** (Left) J/V curves and (right) IPCE spectra of the p -DSCs employing bare electrodes with different doping degree: 0%
351 (black), 0.1% (light blue), 1% (dark blue), 2% (orange), 5% (red) and 10% (green).

352 By definition the IPCE (Incident Photo-to-current Conversion Efficiency) is the ratio of the number
353 of collected carriers to the number of all the incident photons on the device active area at a given
354 wavelength. The differences in the spectra reported in figure 7 evidence that the probability with
355 which the photoinjected holes reach the current collector (η_{tr}) varies with the content of zirconia
356 and follows the trend of the photocurrent, i.e. the higher the photocurrent powered by the device,
357 the higher the maximum of the IPCE spectra. Some little shifts of the wavelength corresponding to
358 IPCE maximum are expected for the different electrodes due to the blue-shift of the optical bandgap
359 introduced by the presence of zirconia, as previously outlined.

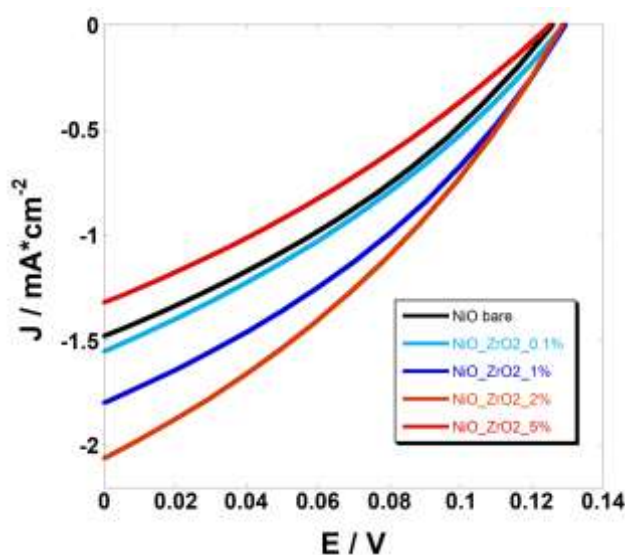
360 P1 was the sensitizer of our p -DSCs³⁶ (sensitization conditions: 16 hours in a 0.3 mM solution of
361 the dye in ACN). NiO_ZrO₂_10% has been excluded from the analyses because of its poor
362 electrochemical and photoelectrochemical performance. Upon sensitization the enhancement of the
363 photocurrent is clear in going from NiO to NiO_ZrO₂_2%. Yet the magnitude of such an increase is
364 lower compared to the corresponding increase when un-sensitized electrodes are employed (+ 46%
365 vs +123%, respectively). This difference was mainly due to the presence of the sensitizer: the dye
366 partially acts as a passivating agent by reducing the free Ni³⁺ sites that represent the actual sites of
367 anchoring. Some of the Ni³⁺ sites are actively involved in binding P1 onto the NiO surface, whereas
368 other are simply covered as a consequence of the steric hindrance of the organic molecule. J_{sc}
369 values varied from 1.447 mA cm^{-2} to 2.037 mA cm^{-2} in passing from bare NiO to NiO_
370 ZrO₂_0.020. To our knowledge the efficiency value of 0.088% here obtained with P1-sensitized
371 NiO_ZrO₂_0.020. is the highest reported for a P1-sensitized screen-printed NiO electrode without
372 the integration of a NiO compact layer^{37,38}. NiO_ZrO₂_0.1% and NiO_ZrO₂_1% have shown quite
373 similar performances (1.611 and 1.690 mA cm^{-2} of short circuit current density, respectively) but
374 far from the record value.

375

	Dye	$J_{sc}/ \text{mA} \cdot \text{cm}^{-2}$	V_{oc} / mV	FF / %	$\eta / \%$	Dye Loading / $10^8 \cdot \text{mmol} \cdot \text{cm}^{-2}$
NiO	-	0.448 ± 0.012	83 ± 2	33.8 ± 0.9	0.012	-
NiO_ZrO ₂ _0.001	-	0.480 ± 0.020	83 ± 2	34.1 ± 0.7	0.014	-
NiO_ZrO ₂ _0.010	-	0.618 ± 0.023	78 ± 1	33.2 ± 0.7	0.016	-
NiO_ZrO ₂ _0.020	-	0.994 ± 0.033	78 ± 2	33.7 ± 0.6	0.026	-
NiO_ZrO ₂ _0.053	-	0.747 ± 0.028	75 ± 3	27.9 ± 0.9	0.017	-
NiO_ZrO ₂ _0.111	-	0.414 ± 0.056	84 ± 3	25.3 ± 0.8	0.009	-
NiO	P1	1.447 ± 0.120	129 ± 2	32.5 ± 0.6	0.060	3.19 ± 0.62
NiO_ZrO ₂ _0.001	P1	1.611 ± 0.089	130 ± 2	32.4 ± 0.5	0.068	3.16 ± 0.52
NiO_ZrO ₂ _0.010	P1	1.690 ± 0.103	130 ± 3	34.4 ± 0.5	0.075	3.27 ± 0.39
NiO_ZrO ₂ _0.020	P1	2.037 ± 0.095	129 ± 2	33.6 ± 0.6	0.088	3.22 ± 0.41
NiO_ZrO ₂ _0.053	P1	1.313 ± 0.063	126 ± 1	30.5 ± 0.3	0.050	2.65 ± 0.53
NiO_ZrO ₂ _0.111	P1	-	-	-	-	-

376 **Table 3.** Photoelectrochemical parameters of the *p*-DSCs with the differently doped ZrO₂-NiO nanocomposite photoelectrodes. The
377 reported values are obtained from averaging the performances of five devices. The errors on the efficiency values are lower than
378 0.001 and have not been reported.

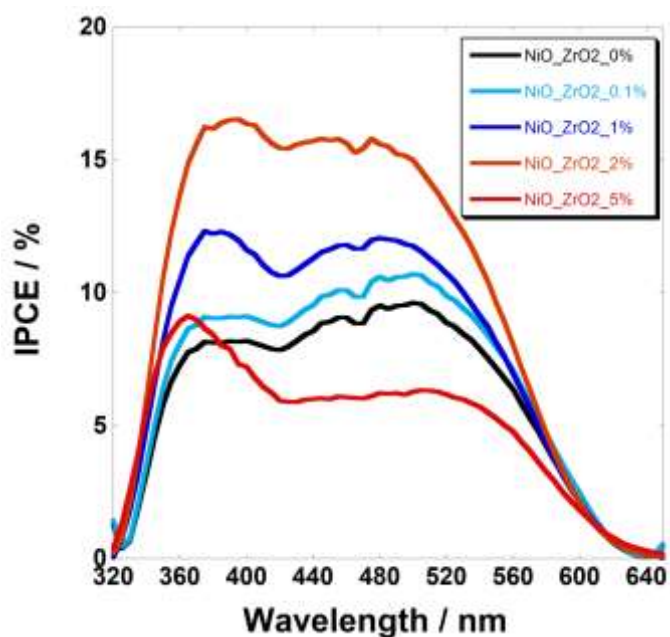
379



380

381 **Figure 8.** JV curves of the complete devices built up with P1-sensitized electrodes with different doping degree: 0% (black), 0.1%
382 (light blue), 1% (dark blue), 2% (orange) and 5% (red).

383 NiO_ZrO₂_5% displayed the worst performance in terms of current density and open circuit
384 voltage. The lower values of J_{sc} , V_{oc} and FF are mainly due to an insufficient dye-loading (see
385 Table 3): zirconia macrostructures, even if they are not as extended as in case of NiO_ZrO₂_10%
386 (see SEM pictures in Figure 2), seem to prevent the full penetration of the sensitizer throughout the
387 porous structure of the electrode with consequent insufficient dye-loading. Similar to not sensitized
388 devices, no substantial variations of V_{oc} could be observed. The highest values of fill factor (34.4%
389 and 33.6%), have been reported when the fraction of ZrO₂ are 1% and 2%. This evidence confirms
390 the optimal dispersion of zirconia NPs in the fraction range of 1-2 % as already outlined by the
391 electrochemical measurements. IPCE spectra of the P1-sensitized devices (Figure 9), confirmed the
392 trend shown by JV curves.



393

394 **Figure 9.** IPCE spectra of the complete devices built up with P1-sensitized electrodes with different doping degree: 0% (black), 0.1%
 395 (light blue), 1% (dark blue), 2% (orange) and 5% (red).

396 The different performances of the *p*-DSCs differing for the composition of the nanocomposite
 397 electrodes could be ascribed to a minimization of the recombination reactions involving the reduced
 398 species in the electrolyte, i.e. I^- , and the surface localized holes in the NiO electrode. The similar
 399 values of dye loading and bandgap for the series of electrodes here considered indicate that the
 400 kinetics of charge injection is not sensibly altered by the fraction of zirconium oxide. The
 401 electrochemical impedance spectra of the different photoelectrochemical cells are presented in Figure
 402 9. For sake of simplicity the impedance spectrum of the DSC with NiO_ZrO₂_0.1% photocathode is
 403 not shown due to the similarity with the spectrum of the cell having sole NiO photocathode.

404 The electric parameters reported in Table 4 could be extracted from experimental data when the
 405 equivalent circuit²⁸ of the inset of Figure 10 is adopted as model. In this model R_s is the resistance
 406 of all the external elements. It should be constant within the experimental error. R_{CE} is the resistance
 407 of charge transfer through the electrolyte/counter electrode interface and corresponds to the process
 408 of oxidation of the reduced species of the redox shuttle (i.e. I^-) at Pt electrode. C_{CE} is the capacitance
 409 at the electrolyte/counter electrode interface. The following circuitual elements have been defined in
 410 the transmission line element adapted by Bisquert to analyze the impedance response of *n*-type
 411 DSCs³⁹ and successfully employed for the analysis of the impedance spectra of *p*-type DSCs²⁸:

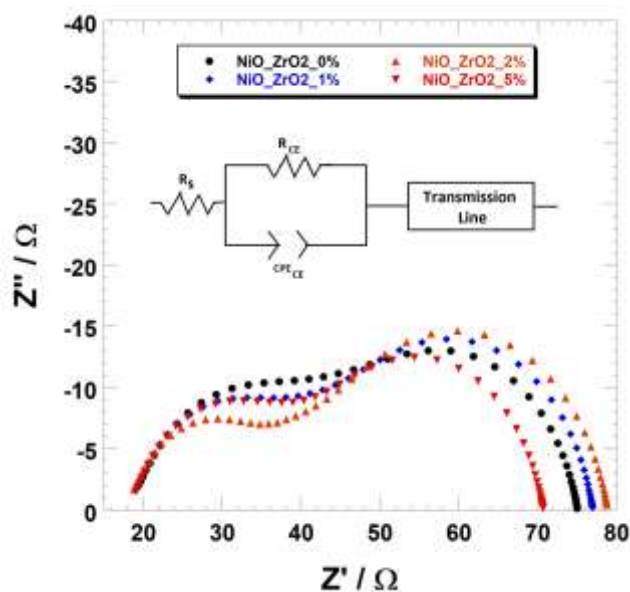
- 412 • R_t is the (transport) resistance of the electronic charge carriers, i.e the holes, to traverse the
 413 NiO electrode and reach the FTO back contact (charge collector).
- 414 • R_{rec} is the resistance of recombination the charge carriers experience after photogeneration.
 415 Patterns of recombination can be due either to the recombination of the excited/oxidized dye
 416 with the hole or to the recombination of the photogenerated hole with a reducing species in
 417 the electrolyte, namely I^- .
- 418 • C_μ is the (chemical) capacitance of the NiO-based photocathode and is related to the content
 419 of charge that is present inside the illuminated photocathode.

420 The employment of the transmission line element is consistent with the mesoporous nature of the
 421 photocathodes. The pure capacitive elements are here replaced with the CPE (constant phase

422 element) that allows an easier fit of the experimental data without influencing the reliability of the
 423 obtained parameters. The actual capacitance (C_{real}) could be calculated applying the following
 424 equation:

$$425 \quad C_{real} = \frac{(C_{CPE} * R)^{\left(\frac{1}{n}\right)}}{R}$$

426 in which C_{CPE} and n are the two parameters describing the capacitive properties of the CPE element
 427 whilst R is the value of the resistance associated to CPE. If n is equal to 1, the CPE acts a pure
 428 capacitance.



429
 430 **Figure 10.** EIS spectra of the complete devices built up with P1-sensitized electrodes differing for the fraction of zirconia dopant: 0%
 431 (black dots), 1% (dark blue diamonds), 2% (orange triangles) and 5% (red triangles). In the inset, the equivalent circuit employed for
 432 the experimental data interpolation is reported.

433 The determination of these electrical parameters allows the direct calculation of the following
 434 microscopic parameters:

- 435 • $\tau_h (= R_t * C_{\mu})$, i.e. the time the photoinjected holes take to reach the FTO charge collector;
- 436 • $\tau_{rec} (= R_{rec} * C_{\mu})$, i.e. the holes lifetime that corresponds to the time the photoinjected holes
 437 spend before undergoing any type of recombination process;
- 438 • $L_h [= l (R_t/R_{rec})^{1/2}]$, where l is the nominal film thickness] is the mean free path of the
 439 photoinjected holes before being involved in recombination reactions;
- 440 • $D_h (=L_h^2 / \tau_h)$ is the average diffusion coefficient of the photoinjected holes through the
 441 photocathode.

442 The values of both R_{CE} and C_{CE} did not vary considerably with the concentration of ZrO_2 NPs in the
 443 nanocomposite electrode. The modification in electronic and photoelectronic properties of the
 444 working photoelectrode do not influence the kinetics of charge transfer processes at the counter-
 445 electrode.

446 In the p -DSCs the value of R_t decreased with the increase of ZrO_2 molar content in the
 447 photocathode in agreement with the ameliorated electronic transport properties of the NiO electrode

448 due to the controlled doping with zirconia when the three-electrode cell was analyzed. The presence
 449 of zirconia NPs onto the NiO surface reduces the number of free trap sites (i.e. Ni³⁺ surface located
 450 sites) which contribute to the chemical capacitance of the electrode. This is proved by the higher
 451 value of C_μ reported for NiO_ZrO₂_1% and NiO_ZrO₂_2% (101 μF and 115 μF, respectively)
 452 compared to the un-doped NiO electrode (89 μF). The relatively low value of chemical capacitance
 453 (i.e. 97 μF) recorded for NiO_ZrO₂_5% is probably due to the insufficient dye loading that prevents
 454 the photoinjection of a high number of carriers. The low value of R_{rec} for the NiO_ZrO₂_5%
 455 electrode is associated with a relatively low amount of dye. Both un-doped NiO and NiO_ZrO₂_5%
 456 electrode showed the lowest R_{rec} values (56.3 Ω and 57.3 Ω, respectively) while NiO_ZrO₂_1%
 457 with 63.8 Ω and NiO_ZrO₂_2% with 70.3 Ω gave the best performing cells in combination with
 458 the higher resistance of recombination (see *JV* curves in Figure 7). The analysis of the data showed
 459 a linear correlation between R_{rec} and J_{SC}: the higher the former the higher the latter. Such a linear
 460 correlation does not hold when η is correlated to R_{rec} (and J_{SC}). The values of τ_{rec} followed the same
 461 trend of R_{rec}. A remarkably long time of recombination of 8.1 ms for the charge carriers diffusing
 462 through NiO_ZrO₂_2% has been found in combination with long diffusion length (3.7 μm) and high
 463 diffusion coefficient (5.7 *10⁻⁵ cm² s⁻¹). This is a consequence of the fact that the photoinjected
 464 holes have a longer mean free path and a higher rate of diffusion throughout the NiO film in
 465 presence of zirconia nanoparticles with respect to undoped NiO. The Ni³⁺ trap states are expected to
 466 be masked and eventually annihilated upon addition of zirconia nanoparticles. For the confirmation
 467 of the latter statement the analysis of the surface with XPS will be necessary and is planned in a
 468 successive study. The photoelectrode formulation NiO_ZrO₂_5% presented a low value of τ_{rec}, as
 469 well as the lowest value of τ_h within the series of the electrodes. It is expected that such a content of
 470 zirconia prevents the homogeneous sensitization of the anchoring sites of NiO, which also behave
 471 as trapping species. Such sites in the not sensitized state contribute to lower the hole diffusion time
 472 with the consequent attainment of high values of D_h (Table 4).
 473

ZrO ₂ (%)	0	1	2	5
R _{CE} (Ω)	13.0 ± 0.1	13.3 ± 0.2	13.0 ± 0.1	12.8 ± 0.1
C _{CE} (μF)	12.7 ± 0.3	13.1 ± 0.2	12.4 ± 0.2	12.3 ± 0.1
R _t (Ω)	27.3 ± 0.5	23.0 ± 0.4	20.8 ± 0.2	18.6 ± 0.5
R _{rec} (Ω)	56.3 ± 0.5	63.8 ± 0.8	70.3 ± 0.7	57.3 ± 0.8
C _μ (μF)	89 ± 3	101 ± 3	115 ± 4	97 ± 3
τ _h (ms)	2.4 ± 0.1	2.3 ± 0.1	2.3 ± 0.1	1.8 ± 0.1
τ _{rec} (ms)	5.0 ± 0.1	6.4 ± 0.2	8.1 ± 0.1	5.6 ± 0.1
L _h (μm)	2.9 ± 0.3	3.3 ± 0.2	3.7 ± 0.2	3.5 ± 0.2
D _h (cm ² /s) *10 ⁻⁵	3.4 ± 0.1	4.8 ± 0.2	5.7 ± 0.2	6.9 ± 0.3

474 **Table 4.** Microscopic parameters with the relative errors as determined by the interpolation of EIS spectra of Figure 9. The
 475 reported values are averaged considering the measurements conducted on five different cells with the photoelectrodes from the same
 476 batch.

477 Treatments like the deposition of a blocking layer between the FTO and the photocathode or the
 478 post-sintering surface modification of NiO based electrodes are expected to further enhance the
 479 performance of *p*-DSCs. For this reason, further experiments in the direction of the modification of
 480 the photocathode with inclusion of a blocking compact layer and consideration of post deposition
 481 treatments will be planned. The main motivation of the conduction of this type of studies is the
 482 implementation of the best performing photocathodes in tandem DSCs when comparable current

483 densities and efficiencies are achieved at the corresponding photoelectrodes of *p*- and *n*-type
484 devices.

485

486 CONCLUSIONS

487 The nanocomposites obtained from the sintering of nanoparticles (NPs) of nickel oxide (NiO) and
488 zirconia (ZrO₂) have been employed as photocathodes of *p*-type dye-sensitized solar cells (*p*-
489 DSCs), P1 being the sensitizer. NiO represented the component in large excess whereas ZrO₂
490 constituted the doping species of the nanocomposite with a percentage of less than 10%. Nano-
491 dispersed ZrO₂ minimized recombination phenomena at the electrode/electrolyte interface of the *p*-
492 DSC when the redox shuttle was the couple I⁻/I₃⁻. The best performance of the photoelectrochemical
493 cell was obtained with the electrode having the 2% of ZrO₂ in the NiO matrix. **This enhancement**
494 **(due to the addition a controlled amount of ZrO₂ NPs) was firstly ascribed to a minimization of the**
495 **recombination phenomena occurring at the electrode/dye/electrolyte interface. Electrochemical**
496 **impedance measurements were employed to prove this hypothesis: recombination resistance was**
497 **improved by 25% (from 56.3 to 70.3 Ω); additionally, hole transport resistance was reduced to 20.8**
498 **Ω (from 27.3 Ω of bare NiO). These evidences lead to slower recombination time, faster hole**
499 **transport, longer hole diffusion length and higher diffusion coefficient.** The efficiencies of the *p*-
500 DSCs with NiO/ ZrO₂ nanocomposites were 123% and 48% higher than un-doped NiO for the bare
501 and sensitized electrode, respectively. SEM-EDX experiments have been performed to visualize the
502 pattern of dispersion of ZrO₂ NPs in the NiO matrix. The values of 0.1 and 1% of zirconia do not
503 assure a uniform dispersion. When the concentration of zirconia was higher than 5%, the NPs
504 merged to form macrostructures. This phenomenon of ZrO₂ NPs aggregation on the electrode
505 surface prevented surface passivation and efficient dye-loading. The enhancement here reported
506 consists in a considerable breakthrough as far as the lowering of charge recombination phenomena
507 *p*-DSCs is concerned. On the other hand, the optimization of the other cell elements, e.g. dye,
508 electrolyte etc., will be mandatory to further improve the conversion performance of this type of
509 devices in perspective of assembling tandem devices with nanocomposite photocathodes.

510

511 ACKNOWLEDGMENTS

512 The authors acknowledge the financial support from MIUR which funded the research project PRIN
513 2010–2011 (protocol no. 20104XET32). DD acknowledges the financial support from the
514 University of Rome “LA SAPIENZA” through the program Ateneo 2012 (Protocol No.
515 C26A124AXX). A.D.C. thanks Regione Lazio and CHOSE for the technical support of the research
516 conducted at the University of Rome “Tor Vergata”. ADC gratefully acknowledges the financial
517 support of the Ministry of Education and Science of The Russian Federation in the framework of
518 Increase Competitiveness Program of NUST «MISiS» (No K2-2017- 025), implemented by a
519 governmental decree dated 16th of March 2013, N 211. Moreover, the authors thank the Center for
520 Nanotechnology Applied to Engineering (CNIS) of the University of Rome LA SAPIENZA for
521 supporting the research and providing access to the DaVinci D8 diffractometer. Authors gratefully
522 acknowledge Prof. Ruggero Caminiti (Director of CNIS Research Centre) for profitable discussion.

523

524

525 REFERENCES

- 527 (1) Yang, W. S.; Park, B. W.; Jung, E. H.; Jeon, N. J.; Kim, Y. C.; Lee, D. U.; Shin, S. S.; Seo, J.; Kim, E. K.; Noh, J. H.; et al.
528 Iodide Management in Formamidinium-Lead-Halide-Based Perovskite Layers for Efficient Solar Cells. *Science* (80-.).
529 **2017**, 356 (6345), 1376–1379.
- 530 (2) Hagfeldt, A.; Boschloo, G.; Sun, L.; Kloo, L.; Pettersson, H. Dye-Sensitized Solar Cells. *Chem. Rev.* **2010**, 110 (11), 6595–
531 6663.
- 532 (3) Kakiage, K.; Aoyama, Y.; Yano, T.; Oya, K.; Kyomen, T.; Hanaya, M. Fabrication of a High-Performance Dye-Sensitized
533 Solar Cell with 12.8% Conversion Efficiency Using Organic Silyl-Anchored Dyes. *Chem. Commun.* **2015**, 51 (29), 6315–
534 6317.
- 535 (4) Freitag, M.; Teuscher, J.; Saygili, Y.; Zhang, X.; Giordano, F.; Liska, P.; Hua, J.; Zakeeruddin, S. M.; Moser, J.-E.; Grätzel,
536 M.; et al. Dye-Sensitized Solar Cells for Efficient Power Generation under Ambient Lighting. *Nat Phot.* **2017**, 11 (6), 372–
537 378.
- 538 (5) Shockley, W.; Queisser, H. J. Detailed Balance Limit of Efficiency of P-n Junction Solar Cells. *J. Appl. Phys.* **1961**, 32,
539 510–519.
- 540 (6) Perera, I. R.; Daenke, T.; Makuta, S.; Yu, Z.; Tachibana, Y.; Mishra, A.; Bäuerle, P.; Ohlin, C. A.; Bach, U.; Spiccia, L.
541 Application of the Tris(Acetylacetonato)Iron(III)/(II) Redox Couple in p-Type Dye-Sensitized Solar Cells. *Angew. Chemie -*
542 *Int. Ed.* **2015**, 54 (12), 3758–3762.
- 543 (7) Awais, M.; Gibson, E.; Vos, J. G.; Dowling, D. P.; Hagfeldt, A.; Dini, D. Fabrication of Efficient NiO Photocathodes
544 Prepared via RDS with Novel Routes of Substrate Processing for P-Type Dye-Sensitized Solar Cells. *ChemElectroChem*
545 **2014**, 1, 384–391.
- 546 (8) Sheehan, S.; Naponiello, G.; Odobel, F.; Dowling, D. P.; Di Carlo, A.; Dini, D. Comparison of the Photoelectrochemical
547 Properties of RDS NiO Thin Films for P-Type DSCs with Different Organic and Organometallic Dye-Sensitizers and
548 Evidence of a Direct Correlation between Cell Efficiency and Charge Recombination. *J. Solid State Electrochem.* **2015**, 19
549 (4), 975–986.
- 550 (9) Wei, L.; Jiang, L.; Yuan, S.; Ren, X.; Zhao, Y.; Wang, Z.; Zhang, M.; Shi, L.; Li, D. Valence Band Edge Shifts and Charge-
551 Transfer Dynamics in Li-Doped NiO Based p-Type DSSCs. *Electrochim. Acta* **2016**, 188, 309.
- 552 (10) Borgström, M.; Blart, E.; Boschloo, G.; Mukhtar, E.; Hagfeldt, A.; Hammarström, L.; Odobel, F. Sensitized Hole Injection
553 of Phosphorus Porphyrin into NiO: Toward New Photovoltaic Devices. *J. Phys. Chem. B* **2005**, 109 (48), 22928–22934.
- 554 (11) Boschloo, G.; Hagfeldt, A. Characteristics of the Iodide/Triiodide Redox Mediator in Dye-Sensitized Solar Cells. *Acc.*
555 *Chem. Res.* **2009**, 42 (11), 1819–1826.
- 556 (12) Bonomo, M.; Dini, D.; Marrani, A. G. Adsorption Behavior of I³⁻ and I⁻ Ions at a Nanoporous NiO/Acetonitrile Interface
557 Studied by X-Ray Photoelectron Spectroscopy. *Langmuir* **2016**, 32 (44), 11540–11550.
- 558 (13) Gibson, E. A.; Le Pleux, L.; Fortage, J.; Pellegrin, Y.; Blart, E.; Odobel, F.; Hagfeldt, A.; Boschloo, G. Role of the
559 Triiodide/Iodide Redox Couple in Dye Regeneration in p-Type Dye-Sensitized Solar Cells. *Langmuir* **2012**, 28 (15), 6485–
560 6493.
- 561 (14) Bonomo, M.; Saccone, D.; Magistris, C.; Di Carlo, A.; Barolo, C.; Dini, D. Effect of Alkyl Chain Length on the Sensitizing
562 Action of Substituted Non Symmetric Squaraines for P-Type Dye-Sensitized Solar Cells. *ChemElectroChem* **2017**, 4 (9),
563 2385–2397.
- 564 (15) Bonomo, M.; Carella, A.; Centore, R.; Di Carlo, A.; Dini, D. First Examples of Pyran Based Colorants as Sensitizing Agents
565 of P-Type Dye-Sensitized Solar Cells. *J. Electrochem. Soc.* **2017**, 164 (13).
- 566 (16) Ho, P.; Bao, L. Q.; Ahn, K. S.; Cheruku, R.; Kim, J. H. P-Type Dye-Sensitized Solar Cells: Enhanced Performance with a
567 NiO Compact Blocking Layer. *Synth. Met.* **2016**, 217, 314–321.
- 568 (17) Ho, P.; Thogiti, S.; Bao, L. Q.; Cheruku, R.; Ahn, K. S.; Hong Kim, J. Enhanced Efficiency via Blocking Layers at
569 Photocathode Interfaces in Cobalt-Mediated Tandem Dye-Sensitized Solar Cells. *Sol. Energy* **2018**, 161, 9–16.
- 570 (18) Cameron, P. J.; Peter, L. M. How Does Back-Reaction at the Conducting Glass Substrate Influence the Dynamic
571 Photovoltage Response of Nanocrystalline Dye-Sensitized Solar Cells? *J. Phys. Chem. B* **2005**.
- 572 (19) Natu, G.; Hasin, P.; Huang, Z.; Ji, Z.; He, M.; Wu, Y. Valence Band-Edge Engineering of Nickel Oxide Nanoparticles via
573 Cobalt Doping for Application in p-Type Dye-Sensitized Solar Cells. *ACS Appl. Mater. Interfaces* **2012**, 4 (11), 5922–5929.
- 574 (20) D'Amario, L.; Boschloo, G.; Hagfeldt, A.; Hammarström, L. Tuning of Conductivity and Density of States of NiO
575 Mesoporous Films Used in P-Type DSSCs. *J. Phys. Chem. C* **2014**, 118 (34), 19556–19564.
- 576 (21) Itapu, S.; Khan, K.; Georgiev, D. G. Effect of UV Laser Irradiation on the Properties of NiO Films and ZnO/NiO
577 Heterostructures. In *MRS Advances*; 2016; Vol. 1, pp 293–298.
- 578 (22) Bonomo, M.; Magistris, C.; Buscaino, R.; Fin, A.; Barolo, C.; Dini, D. Effect of Sodium Hydroxide Pretreatment of NiO x
579 Cathodes on the Performance of Squaraine-Sensitized p-Type Dye-Sensitized Solar Cells. *ChemistrySelect* **2018**, 3 (4),
580 1066–1075.
- 581 (23) Langmar, O.; Saccone, D.; Amat, A.; Fantacci, S.; Viscardi, G.; Barolo, C.; Costa, R. D.; Guldi, D. M. Designing
582 Squaraines to Control Charge Injection and Recombination Processes in NiO-Based Dye-Sensitized Solar Cells.
583 *ChemSusChem* **2017**, 10 (11), 2385–2393.
- 584 (24) Favereau, L.; Pellegrin, Y.; Hirsch, L.; Renaud, A.; Planchat, A.; Blart, E.; Louarn, G.; Cario, L.; Jovic, S.; Boujtita, M.; et
585 al. Engineering Processes at the Interface of P-Semiconductor for Enhancing the Open Circuit Voltage in p-Type Dye-
586 Sensitized Solar Cells. *Adv. Energy Mater.* **2017**, 7 (12), 1601776.
- 587 (25) Uehara, S.; Sumikura, S.; Suzuki, E.; Mori, S. Retardation of Electron Injection at NiO/Dye/Electrolyte Interface by
588 Aluminium Alkoxide Treatment. *Energy Environ. Sci.* **2010**, 3 (5), 641.
- 589 (26) Natu, G.; Huang, Z.; Ji, Z.; Wu, Y. The Effect of an Atomically Deposited Layer of Alumina on NiO in P-Type Dye-
590 Sensitized Solar Cells. *Langmuir* **2012**, 28 (1), 950–956.
- 591 (27) Otroshchenko, T. P.; Turakulova, A. O.; Voblikova, V. A.; Sabitova, L. V.; Kutsev, S. V.; Lunin, V. V. NiO and ZrO₂-
592 Based Catalysts in the Reaction of Complete Methane Oxidation. *Russ. J. Phys. Chem. A* **2013**, 87 (11), 1804–1808.
- 593 (28) Bonomo, M.; Naponiello, G.; Venditti, I.; Zardetto, V.; Carlo, A. Di; Dini, D.; Di Carlo, A.; Dini, D. Electrochemical and

- 594 Photoelectrochemical Properties of Screen-Printed Nickel Oxide Thin Films Obtained from Precursor Pastes with Different
595 Compositions. *J. Electrochem. Soc.* **2017**, *164* (2), H137–H147.
- 596 (29) Ito, S.; Chen, P.; Comte, P.; Nazeeruddin, M. K.; Liska, P.; Péchy, P.; Grätzel, M. Fabrication of Screen-Printing Pastes
597 from TiO₂ Powders for Dye-Sensitized Solar Cells. *Prog. Photovoltaics Res. Appl.* **2007**, *15*, 603–612.
- 598 (30) Qin, P.; Zhu, H.; Edvinsson, T.; Boschloo, G.; Hagfeldt, A.; Sun, L. Design of an Organic Chromophore for P-Type Dye-
599 Sensitized Solar Cells. *J. Am. Chem. Soc.* **2008**, *130*, 8570–8571.
- 600 (31) Mariani, P.; Vesce, L.; Di Carlo, A. The Role of Printing Techniques for Large-Area Dye Sensitized Solar Cells. *Semicond.*
601 *Sci. Technol.* **2015**, *30* (10), 104003.
- 602 (32) Novelli, V.; Awais, M.; Dowling, D. P.; Dini, D. Electrochemical Characterization of Rapid Discharge Sintering (RDS) NiO
603 Cathodes for Dye-Sensitized Solar Cells of p-Type. *Am. J. Anal. Chem.* **2015**, *6* (2), 176–187.
- 604 (33) Wood, C. J.; Summers, G. H.; Clark, C. A.; Kaeffer, N.; Braeutigam, M.; Carbone, L. R.; D’Amario, L.; Fan, K.; Farré, Y.;
605 Narbey, S.; et al. A Comprehensive Comparison of Dye-Sensitized NiO Photocathodes for Solar Energy Conversion. *Phys.*
606 *Chem. Chem. Phys.* **2016**, *18*, 10727–10738.
- 607 (34) Bonomo, M.; Naponiello, G.; Dini, D. Oxidative Dissolution of NiO in Aqueous Electrolyte: An Impedance Study. *J.*
608 *Electroanal. Chem.* **2018**, *816*, 205–214.
- 609 (35) Kumar, K. D. A.; Valanarasu, S.; Jeyadheepan, K.; Kim, H. S.; Vikraman, D. Evaluation of the Physical, Optical, and
610 Electrical Properties of SnO₂: F Thin Films Prepared by Nebulized Spray Pyrolysis for Optoelectronics. *J. Mater. Sci.*
611 *Mater. Electron.* **2018**, *29* (5), 3648–3656.
- 612 (36) Qin, P.; Wiberg, J.; Gibson, E. A.; Linder, M.; Li, L.; Brinck, T.; Hagfeldt, A.; Albinsson, B.; Sun, L. Synthesis and
613 Mechanistic Studies of Organic Chromophores with Different Energy Levels for P-Type Dye-Sensitized Solar Cells. *J.*
614 *Phys. Chem. C* **2010**, *114* (10), 4738–4748.
- 615 (37) Koussi-Daoud, S.; Planchat, A.; Renaud, A.; Pellegrin, Y.; Odobel, F.; Pauporté, T. Solvent-Templated Electrodeposition of
616 Mesoporous Nickel Oxide Layers for Solar Cell Applications. *ChemElectroChem* **2017**, *4* (10), 2618–2625.
- 617 (38) Klein, Y. M.; Marinakis, N.; Constable, E. C.; Housecroft, C. E. A Phosphonic Acid Anchoring Analogue of the Sensitizer
618 P1 for P-Type Dye-Sensitized Solar Cells. *Crystals* **2018**, *8* (10), 389.
- 619 (39) Fabregat-Santiago, F.; Garcia-Belmonte, G.; Bisquert, J.; Zaban, A.; Salvador, P. Decoupling of Transport, Charge Storage,
620 and Interfacial Charge Transfer in the Nanocrystalline TiO₂/Electrolyte System by Impedance Methods. *J. Phys. Chem. B*
621 **2002**.
- 622
- 623